

## Journal of Turbulence

Publication details, including instructions for authors and  
subscription information:

<http://www.tandfonline.com/loi/tjot20>

### Evolutionary optimization of an anisotropic compliant surface for turbulent friction drag reduction

Koji Fukagata <sup>a</sup>, Stefan Kern <sup>b</sup>, Philippe Chatelain <sup>b</sup>, Petros  
Koumoutsakos <sup>b</sup> & Nobuhide Kasagi <sup>c</sup>

<sup>a</sup> Department of Mechanical Engineering, Keio University, Hiyoshi  
3-14-1, Kohoku-ku, Yokohama, 223-8522, Japan

<sup>b</sup> Chair of Computational Science, ETH Zürich, CH-8092,  
Switzerland

<sup>c</sup> Department of Mechanical Engineering, The University of  
Tokyo, Hongo 7-3-1, Bunkyo-ku, Tokyo, 113-8656, Japan

Published online: 17 Oct 2008.

To cite this article: Koji Fukagata, Stefan Kern, Philippe Chatelain, Petros Koumoutsakos & Nobuhide Kasagi (2008) Evolutionary optimization of an anisotropic compliant surface for turbulent friction drag reduction, Journal of Turbulence, 9, N35

To link to this article: <http://dx.doi.org/10.1080/14685240802441126>

PLEASE SCROLL DOWN FOR ARTICLE

Taylor & Francis makes every effort to ensure the accuracy of all the information (the "Content") contained in the publications on our platform. However, Taylor & Francis, our agents, and our licensors make no representations or warranties whatsoever as to the accuracy, completeness, or suitability for any purpose of the Content. Any opinions and views expressed in this publication are the opinions and views of the authors, and are not the views of or endorsed by Taylor & Francis. The accuracy of the Content should not be relied upon and should be independently verified with primary sources of information. Taylor and Francis shall not be liable for any losses, actions, claims, proceedings, demands, costs, expenses, damages, and other liabilities whatsoever or howsoever caused arising directly or indirectly in connection with, in relation to or arising out of the use of the Content.

This article may be used for research, teaching, and private study purposes. Any substantial or systematic reproduction, redistribution, reselling, loan, sub-licensing, systematic supply, or distribution in any form to anyone is expressly forbidden. Terms &



## Evolutionary optimization of an anisotropic compliant surface for turbulent friction drag reduction

Koji Fukagata<sup>a\*</sup>, Stefan Kern<sup>b</sup>, Philippe Chatelain<sup>b</sup>, Petros Koumoutsakos<sup>b</sup>  
and Nobuhide Kasagi<sup>c</sup>

<sup>a</sup>Department of Mechanical Engineering, Keio University, Hiyoshi 3-14-1, Kohoku-ku, Yokohama 223-8522, Japan; <sup>b</sup>Chair of Computational Science, ETH Zürich, CH-8092, Switzerland; <sup>c</sup>Department of Mechanical Engineering, The University of Tokyo, Hongo 7-3-1, Bunkyo-ku, Tokyo 113-8656, Japan

Direct numerical simulation (DNS) of the channel flow with an anisotropic compliant surface is performed in order to investigate its drag reduction effect in a fully developed turbulent flow. The computational domain is set to be  $3\delta \times 2\delta \times 3\delta$ , where  $\delta$  is the channel half-width. The surface is passively driven by the pressure and wall-shear stress fluctuations, and the surface velocity provides a boundary condition for the fluid velocity field. An evolutionary optimization method (CMA-ES) is used to optimize the parameters of the anisotropic compliant surface. The optimization identifies several sets of parameters that result in a reduction of the friction drag with a maximum reduction rate of 8%. The primary mechanism for drag reduction is attributed to the decrease of the Reynolds shear stress (RSS) near the wall induced by the kinematics of the surface. The resultant wall motion is a uniform wave traveling downstream. The compliant wall, with the parameters found in the optimization study, is also tested in a computational domain that is doubled in the streamwise direction. The drag, however, is found to increase in the larger computational domain due to excessively large wall-normal velocity fluctuations.

**Keywords:** turbulence control; drag reduction; compliant surface; direct numerical simulation; evolutionary optimization

### 1. Introduction

Compliant surfaces have attracted considerable attention as potential passive mechanisms to reduce turbulent friction drag. For laminar-turbulent transition, several theoretical and experimental studies have been reported (see Gad-el-Hak [1] and references therein), and it is now believed that such surfaces can suppress flow instabilities and delay transition. For fully developed wall-bounded turbulent flow, however, drag reduction effect by compliant surfaces has been in question for long time.

Recently, several direct numerical simulation (DNS) studies have tried to clarify whether and how the friction drag is reduced by compliant surfaces. Endo and Himeno [2] performed DNS of turbulent channel flow with a simplified isotropic compliant surface, as shown in Figure 1(b), which models Kramer's coating (Figure 1(a)), and reported a 2.7% drag reduction. This result was soon disproved by a similar DNS by Xu et al. [3], in which no clear drag reduction effect was obtained. The major difference between Endo and Himeno [2] and Xu et al. [3] is the integration time for sampling data;  $t^{+0} = 0\text{--}1000$  in the former and  $t^{+0} = 500\text{--}3000$  in the latter (where

---

\*Corresponding author. Email: fukagata@mech.keio.ac.jp

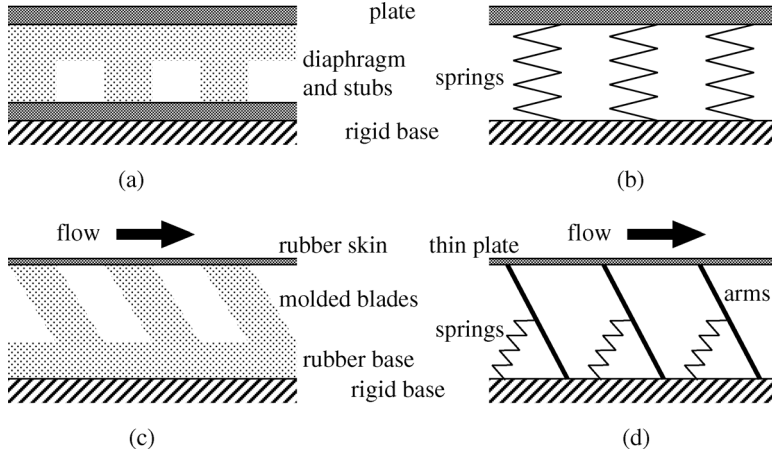


Figure 1. Schematics of compliant walls and their models (redrawn based on Gad-el-Hak [1]). (a) Kramer's coating. (b) Isotropic compliant wall model. (c) Grosskreutz's anisotropic compliant wall. (d) Anisotropic compliant wall model.

the superscript “+0” denotes the wall unit in the case of solid channel). Xu et al. [3] concluded that the drag reduction observed by Endo and Himeno [2] was merely a transitional one. More importantly, their analysis clearly shows that the pressure fluctuation and the wall deformation cannot be in phase, although these should become in phase in order to reduce the drag. This analysis implies that one may need a driving force other than the pressure fluctuations in order to have a surface motion that reduces the friction drag.

In the present study, we perform DNS of channel flow with a compliant surface. In contrast to the previous DNS studies, we consider an anisotropic compliant surface model, as shown in Figure 1(d), which was introduced by Carpenter and Morris [4] to represent Grosskreutz's compliant wall (Figure 1(c)). This anisotropic surface has, at least, two distinct features when compared to the isotropic one:

- (1) The surface is driven not only by the wall pressure, but also by the wall-shear stress fluctuations;
- (2) Due to the constraint of rigid arms, as shown in Figures 1(d) and 2, the wall moves so as to weaken the RSS,  $-\overline{u'v'}$ .

The latter difference is directly related to the reduction of friction drag because of the identity between the RSS and the skin friction coefficient,  $C_f$ , [5, 6], i.e.,

$$C_f = \frac{12}{Re_b} + 24 \int_0^1 (1-y) (-\overline{u'v'}) dy. \quad (1)$$

This is the identity equation for channel flows and all the variables are made dimensionless by using the channel half-width,  $\delta$ , and twice the bulk mean velocity,  $2U_b$ . Note that  $Re_b = 2U_b\delta/\nu$  is the Reynolds number, and  $y$  denotes the distance from the wall. Equation (1) indicates that the skin friction coefficient is decomposed into two parts: one is the laminar contribution given by the well-known laminar solution, and the other is the turbulent contribution, which is proportional to the weighted integral of the RSS. The weighting factor  $(1-y)$  indicates that the RSS near the

wall is more responsible for the friction drag than that in the central region. Therefore, the most straightforward strategy for friction drag reduction is to reduce the RSS in the region near the wall. In fact, this strategy has been verified in the closed-loop control by Fukagata and Kasagi [7] as well as in the open-loop control by Min et al. [8].

Although the above-mentioned motion of the anisotropic compliant wall always produces negative RSS on the wall, the RSS in the near-wall layer is determined as a solution of the Navier–Stokes equation. Namely, it is not known *a priori* whether the friction drag (or, equivalently, the second term of Equation (1)) can be reduced by using an anisotropic compliant wall.

## 2. Anisotropic compliant wall model

### 2.1. Equation of motion

Figure 2 shows again the anisotropic compliant wall model considered in the present study. The movement of the arm is restricted in the  $x$ – $y$  plane parallel to the mean flow direction. Assuming a small change in the arm angle,  $\delta\theta$ , from the equilibrium angle,  $\theta$ , the governing equation for the surface can be written for a single variable,  $\eta_f(x, z, t)$ , as [4]

$$\eta_f = l\delta\theta, \quad (2)$$

where  $l$  is the arm length. The displacement ( $x'_w, y'_w, z'_w$ ) and the velocity ( $u'_w, v'_w, w'_w$ ) of the membrane are given by

$$x'_w = \eta_f \sin \theta, \quad y'_w = \eta_f \cos \theta, \quad z'_w = 0, \quad (3)$$

and

$$u'_w = \frac{\partial \eta_f}{\partial t} \sin \theta, \quad v'_w = \frac{\partial \eta_f}{\partial t} \cos \theta, \quad w'_w = 0, \quad (4)$$

respectively. From Equation (4), the local Reynolds shear stress on the wall due to this surface motion is calculated as

$$-u'_w v'_w = -\frac{\sin(2\theta)}{2} \left( \frac{\partial \eta_f}{\partial t} \right)^2, \quad (5)$$

which is always negative when  $0 < \theta < \pi/2$ .

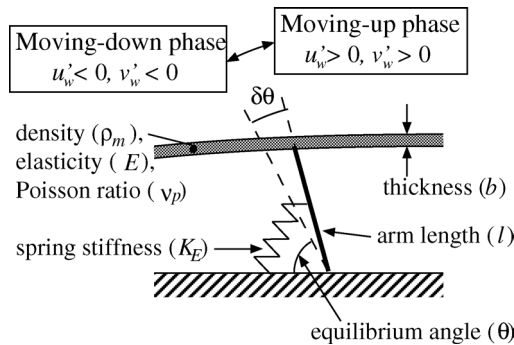


Figure 2. Parameters of the anisotropic compliant wall model.

The governing equation of motion for  $\eta_f$  has been modified from the original [4] so as to allow two-dimensional deformation. Being expressed in wall units, this equation reads

$$\begin{aligned} b^+ \rho_m^+ \frac{\partial^2 \eta_f^+}{\partial t^{+2}} + D^+ \frac{\partial \eta_f^+}{\partial t^+} + B^+ \cos^2 \theta \nabla^{+4} \eta_f^+ \\ - E^+ b^+ \sin^2 \theta \nabla^{+2} \eta_f^+ + K_E^+ \eta_f^+ = f^+, \end{aligned} \quad (6)$$

where

$$f^+ = (-p_w'^+ + \sigma_w'^+) \cos \theta + \tau_w'^+ \sin \theta \quad (7)$$

and  $\nabla^2 = \partial^2/\partial x^2 + \partial^2/\partial z^2$ . The wall unit variants of the membrane parameters are defined by

$$\begin{cases} \rho_m^+ = \frac{\rho_m}{\rho}, & b^+ = \frac{bu_\tau}{v}, & D^+ = \frac{D}{\rho u_\tau}, \\ E^+ = \frac{E}{\rho u_\tau^2}, & K_E^+ = \frac{K_E v}{\rho u_\tau^3}. \end{cases} \quad (8)$$

where  $b$ ,  $\rho_m$ ,  $E$ , and  $K_E$  are the thickness, the density, the elastic modulus of the membrane, and the spring stiffness, respectively. The flexural rigidity of the membrane,  $B$ , in this case is given by

$$B = \frac{Eb^3}{12(1 - v_p^2)}, \quad (9)$$

where  $v_p$  is the Poisson ratio. A damper designed by the parameter  $D$  is added to the spring. The driving forces are fluctuations in the pressure  $p_w'$ , the normal stress,  $\sigma_w'$ , and the shear stress,  $\tau_w'$ .

## 2.2. Monoharmonic analysis

Two-dimensional Fourier transform of the membrane equation of motion results in the equation of motion for the standard spring-mass-damper system, i.e.,

$$\frac{\partial^2 \hat{\eta}_f}{\partial t^2} + 2\zeta \omega_n \frac{\partial \hat{\eta}_f}{\partial t} + \omega_n^2 \hat{\eta}_f = \frac{\hat{f}}{b\rho_m}, \quad (10)$$

where the hat ( $\hat{\cdot}$ ) denotes the Fourier coefficient,

$$\omega_n = \sqrt{\frac{K_E + Bk^4 \cos^2 \theta + Ebk^2 \sin^2 \theta}{b\rho_m}} \quad (11)$$

is the natural angular frequency of the wavenumber-mode  $k$  (with  $k = \sqrt{k_x^2 + k_z^2}$ ) and

$$\zeta = \frac{D}{2b\rho_m\omega_n} \quad (12)$$

is the damping coefficient. From the classical control theory, the gain ( $|\hat{G}(i\omega)|$ ) and phase delay ( $\angle\hat{G}(i\omega)$ ) of the velocity ( $\partial\hat{\eta}_f/\partial t$ ) in response to the force ( $\hat{f}$ ) can be found as

$$|\hat{G}(i\omega)| = \frac{\left(\frac{\omega}{\omega_n}\right)}{b\rho_m \sqrt{\left[1 - \left(\frac{\omega}{\omega_n}\right)^2\right]^2 + \left(2\zeta \frac{\omega}{\omega_n}\right)^2}} \quad (13)$$

and

$$\angle\hat{G}(i\omega) = \tan^{-1} \left[ \frac{1 - \left(\frac{\omega}{\omega_n}\right)^2}{2\zeta \frac{\omega}{\omega_n}} \right], \quad (14)$$

respectively. The form of these equations is exactly the same as that of the isotropic compliant surface [3]. We note, however, that the relationship between the oscillation frequency and the wavenumber (Equation (11)) and the composition of the driving force (Equation (7)) are different.

### 3. Numerical procedure

#### 3.1. Direct numerical simulation

We consider an incompressible turbulent channel flow. The fluid velocity field is simulated by using the second-order finite-difference code, which was originally developed for pipe flows [9] and later adapted to channel flows [10]. The Navier–Stokes equation is discretized by using the energy conservative second-order accurate finite-difference method [11, 12]. Time integration is done by using the low-storage third-order Runge–Kutta/Crank–Nicolson (RK3/CN) scheme (see, e.g., [13]) together with the delta-form fractional step method [14]. The Poisson equation is solved by using the fast Fourier transform in the streamwise ( $x$ ) and spanwise ( $z$ ) directions and the tridiagonal matrix solver in the wall-normal ( $y$ ) direction.

The flow rate is kept constant. The bulk Reynolds number,  $Re_b$ , is 3300, which corresponds to a friction Reynolds number of about 110 ( $Re_\tau = 112.46$ ) in the case of rigid walls. The computational domain is  $3\delta \times 2\delta \times 3\delta$  and the number of cells is  $32 \times 64 \times 64$  in the streamwise ( $x$ ), the wall normal ( $y$ ), and the spanwise ( $z$ ) directions, respectively. This domain size is similar to that used in the previous study of isotropic compliant surfaces by Xu et al. [3].

The membrane equation of motion, Equation (6), is spatially discretized by the second-order accurate finite-difference method on the same mesh as that for the wall boundary of the fluid velocity field. The time integration is done by the RK3/CN method with the same time stepping as that for the fluid. The membrane is driven by the pressure and wall-shear fluctuations, as described by Equations (6) and (7), whereas the velocity of the membrane computed at every instant is used as the boundary condition of the fluid velocity field at the wall, i.e., Equation (4). In order to enable an optimization study, deformation of the membrane is neglected. This simplification is justified when the wall displacement is relatively small (say, less than about 5 wall units). Note that Kang and Choi [15] from their DNS of feedback-controlled channel flow reported that, when the wall displacement is less than the 5 wall units, most of the drag reduction is due to the velocity induced by the wall motion rather than the wall displacement. Miwa [16] studied by means of DNS the velocity induced by a wall deformation and a blowing/suction at the same velocity. He also reports that the effect of displacement is negligibly small when the displacement is on the order of 1 wall unit. These observations are also reasonable from the well-known fact

that the wall with roughness of which grain size is less than 5 wall units can be considered as a hydrodynamically smooth wall.

The computational time step is chosen so that both the Courant-Friedrichs-Lewy (CFL) number for the fluid and that for the membrane (determined by the wavespeed,  $c = \omega_n/k$ ) are less than 0.5.

The computation is started from the velocity field of a solid channel flow and integrated for  $t^{+0} = 0$ –12000. The statistics presented below are accumulated during the time period of  $t^{+0} = 6000$ –12000, which is about twice as long as that used by Xu et al. [3].

### 3.2. Evolutionary optimization

The monoharmonic analysis of the compliant wall model gives us an estimate of the wavelike behavior of the wall, but cannot predict the highly nonlinear interaction of the wall with the turbulent flow. In order to systematically assess the proposed compliant surface design, an inverse design procedure, employing an evolutionary optimization algorithm, is used to find optimal parameters for the model.

The inverse design problem is formulated as an optimization problem. Our objective is to minimize the friction drag coefficient  $C_f$ , which is a function of wall parameters  $\alpha = (b, \rho_m, E, K_E, \theta, D)$ , under the restriction of wall-deformation amplitude. Therefore, the loss function (which is also called as the cost function)  $L$  can be defined here as

$$L(\alpha) = C_f(\alpha) + c_\eta H(\eta_{f,\text{rms}}^{+0}(\alpha) - 5) \times (\eta_{f,\text{rms}}^{+0}(\alpha) - 5)^2. \quad (15)$$

The first term in Equation (15) is the friction drag that we want to minimize. The second term is a penalty term, where  $c_\eta$  is the constant scaling factor and  $H(\cdot)$  is the Heaviside function. This penalty term takes a very large value when the simulation results in the root-mean-square (rms) of  $\eta_f^{+0}$  larger than 5 (i.e., large deformation), so that it works to avoid solutions contradicting the aforementioned assumption.

The turbulent channel flow coupled with the compliant walls is a highly dynamical system that is susceptible to small changes in design parameters requiring an optimization algorithm that is robust in the presence of uncertainties, and possibly, multiple optima. In addition, the algorithm should be highly efficient since the evaluation of  $L(\alpha)$  using DNS is computationally intensive even with the velocity coupling only.

We implement an *Evolution Strategy with Adaptation of the Covariance Matrix* (CMA-ES) [17–19]. The competitive performance and robustness of CMA-ES has been demonstrated in a number of benchmark optimization problems [20] and applications. Based on a preliminary parameter study, we choose a logarithmic encoding for all parameters except  $\theta$ . The search domain is set to be:

$$\begin{cases} \rho_m^{+0} = 1.0 \times 10^{\alpha_1}, & \alpha_1 \in [-1, 1], \\ E^{+0} = 6.3 \times 10^{\alpha_2}, & \alpha_2 \in [-1, 1], \\ K_E^{+0} = 8.2 \times 10^{\alpha_3}, & \alpha_3 \in [-5, -2], \\ \theta = 30 \times \alpha_4 \text{ deg.}, & \alpha_4 \in [1, 3], \\ D^{+0} = 3.0 \times 10^{\alpha_5}, & \alpha_5 \in [-3, -1]. \end{cases} \quad (16)$$



The thickness  $b^{+0}$  is kept constant at  $b^{+0} = 1.1$ .

Similar to other evolution strategies, such as the genetic algorithm, a set of parameters is treated as an individual. The individuals evolve (i.e., the parameters are modified) according to the prescribed rule so as to minimize the loss function  $L$ . The population size  $\lambda$  (i.e., number of individuals per generation) is chosen based on empirical estimates of the order of  $2n$ , where  $n$  is the number of parameters. By using a larger population, we can compensate for multimodal cost functions at the expense of larger numbers of evaluations. Moreover, when the population size is set equal to the number of available processors, the advantage of using CMA-ES can fully be exploited. For the present study, 32 processors were available for parallel function evaluations. Therefore, we chose  $\lambda = 32$  which is four times the default population size for a five-dimensional problem [18]. For more details of the CMA-ES algorithms, the readers are referred to [17–20].

The evaluation of the populations is performed in parallel. The uncertainty in the evaluation of  $C_f(\alpha)$  is reduced by actually performing two evaluations starting from different initial conditions. In addition, the twofold evaluation allows for a simple, yet efficient, load balancing by pairing cases with small and large time-steps on the individual CPUs.

## 4. Results and discussion

### 4.1. Optimization results

The CMA-ES was initialized with sets of parameters distributed over the initial search domain, i.e., Equation (16). The available computation time permitted about 1000 evaluation trials (to be exact, 992 evaluations) of the loss function,  $L(\alpha)$ , each one involving two simulations with different initial turbulent fields (viz., about 2000 DNS runs were made in total). As Figures 3 and 4 imply, the results of the optimization procedure using CMA-ES are ambivalent: while some very promising solutions are found, the algorithm does not show clear signs of converging to an optimal solution within the given number of function evaluations.

Table 1 summarizes three cases. A case consists of a parameter set and the resulting function value. The table shows the two best cases obtained in the present optimization (Cases A1 and A2) and a case of drag increase (Case B). While not far from each other, the actual parameter figures for the two best cases confirm that the algorithm has not converged yet. This also hints at the multimodality of the underlying physics.

The table also shows the resultant drag reduction rate,  $R_D$ , i.e.,

$$R_D = \frac{C_{f0} - C_f}{C_{f0}}, \quad (17)$$

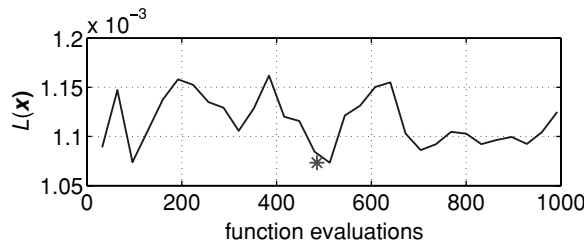


Figure 3. History of loss function,  $L(\alpha)$ , of the best individual in every generation. Since, one generation consists of 32 function evaluations, the value is plotted every 32 evaluations. The star symbol denotes the loss function value of the best parameter set found in the present optimization attempt.

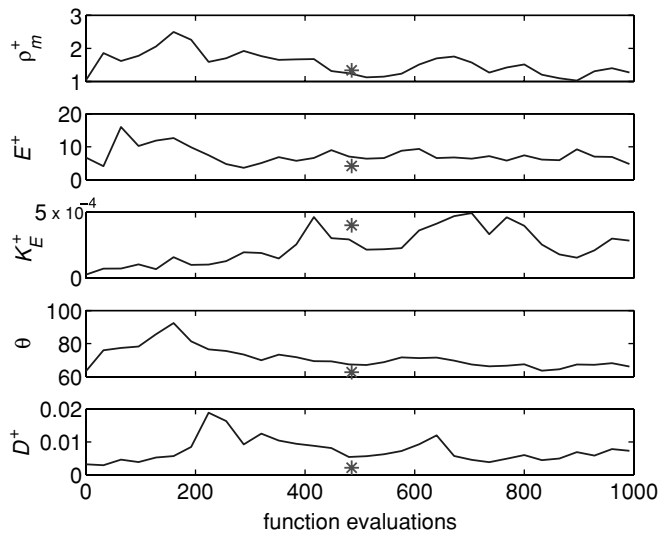


Figure 4. History of the population mean of parameters of the compliant wall. The star symbol denotes the best parameter set found in the present optimization attempt.

(where  $C_{f0}$  denotes  $C_f$  of the solid channel) and the computed root-mean-square (rms) wall displacement ( $y_{\text{rms}}^{+0}$ ). Drag reduction is attained in Cases A1 and A2, and amounts to 7–8%. The time trace of the normalized skin friction coefficient in Figure 5 also confirms the drag reduction in these two cases, although the fluctuation is relatively large due to the intermittency of very low Reynolds number flow and the small computational domain used. An interesting observation in Table 1 is that the equilibrium arm angle ( $\theta$ ) of the best two cases is about  $60^\circ$ , since the optimization has been made in the range of  $30^\circ < \theta < 90^\circ$ . This angle makes the wall structure quite sensitive to the wall shear stress and suggests that this quantity drives motions that play an important role for drag reduction, as anticipated in our comparison with isotropic compliant wall.

The natural angular frequency,  $\omega_n$  (see, Equation (11)), and the damping factor,  $\zeta$  (Equation (12)), of the cases above are shown in Figure 6 as functions of the two-dimensional wavenumber,  $k$ . These surfaces have much lower frequency than the typical frequency of

Table 1. The parameters of two best cases (Cases A1 and A2) and a case of drag increase (Case B) (in wall units of solid channel) and the resultant drag reduction rate ( $R_D$ ) and rms wall displacement ( $y_{w,\text{rms}}^{+0}$ ).

Case	A1	A2	B
$\rho_m^{+0}$	$1.23 \times 10^0$	$1.34 \times 10^0$	$7.42 \times 10^{-1}$
$b^{+0}$	1.1	1.1	1.1
$E^{+0}$	$2.61 \times 10^0$	$4.03 \times 10^0$	$1.12 \times 10^0$
$K_E^{+0}$	$3.25 \times 10^{-4}$	$3.75 \times 10^{-4}$	$8.62 \times 10^{-5}$
$\theta$ [deg.]	62.7	62.7	63.9
$D^{+0}$	$6.49 \times 10^{-4}$	$2.12 \times 10^{-3}$	$1.29 \times 10^{-3}$
$R_D$ [%]	8.32	7.00	−10.7
$y_{w,\text{rms}}^{+0}$	3.67	3.14	6.10

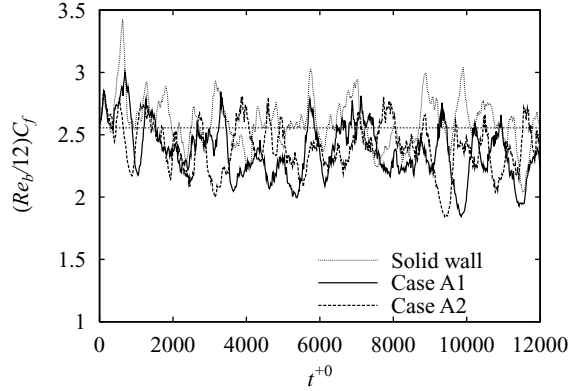


Figure 5. Time trace of the friction drag normalized by the laminar drag.

near-wall turbulence. The damping coefficient is much smaller than unity, and this fact means that the surface is underdamped. From these viewpoints, Case B (which results in drag increase) has similar characteristics to those of Cases A1 and A2. The major difference is that Case B has slightly softer membrane and spring, which result in larger wall displacement,  $y_{\text{rms}}^{+0}$ .

#### 4.2. Turbulence statistics

Figure 7 shows the mean velocity,  $U^{+0}$ , for the three cases in Table 1. The slight increase/decrease of  $U^{+0}$  observed around  $y^{+0} \simeq 1$  simply reflects the drag increase/decrease due to the surface motion, because it is made dimensionless by using the friction velocity of the solid channel. An interesting observation is that the mean velocity around  $y^{+0} \simeq 10$  is slightly reduced as compared

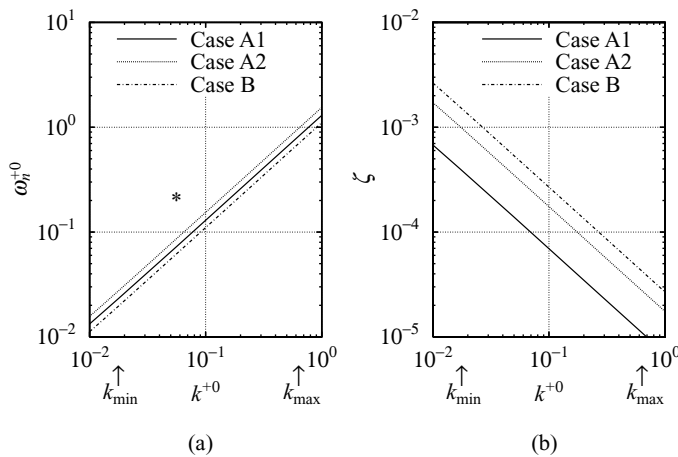


Figure 6. (a) Oscillation frequency ( $\omega_n$ ), and (b) damping coefficient ( $\zeta$ ) as a function of the two-dimensional wavenumber ( $k$ ). The wavenumbers,  $k_{\text{min}}$  and  $k_{\text{max}}$ , denote the minimum and maximum wavenumbers in the present DNS. The asterisk at  $(k^{+0}, \omega^{+0}) = (0.05, 0.2)$  corresponds to the typical scale of near-wall turbulence.

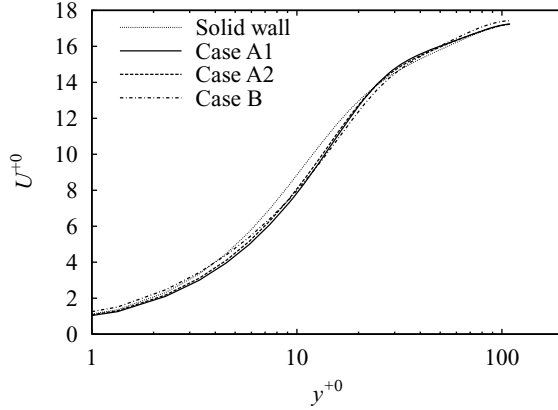


Figure 7. Mean velocity profile. See Table 1 for the description of cases.

to the case of solid wall, both in the drag reducing cases (Cases A1 and A2) and in the drag increasing case (Case B). The reason for this is explained later.

The Reynolds shear stress (RSS) is shown in Figure 8. In all cases, the RSS takes a negative value on the wall. This is actually enforced by the design of the surface; its motion is restricted by the rigid arm (Figure 2). In accordance with the identity Equation (1), the RSS is significantly reduced in Cases A1 and A2, except for the region of  $2 < y^{+0} < 7$ . In Case B, in contrast, the RSS is increased only slightly far from the wall but significantly increased near the wall, so that the drag increases. Note that only the turbulent structure in the region near the wall is modified directly by the wall motion. Similar to the case of blowing and suction from the wall, the changes in the region far from the wall are regarded as indirect effects [21], especially due to the change of mean pressure gradient.

The changes in the RSS profile are mathematically connected to the changes in the mean velocity profile (Figure 7) via (see, Equation (2.4) of [22]):

$$U(y) = Re_b \left[ \underbrace{\frac{C_f}{8} \left( y - \frac{y^2}{2} \right)}_{\text{I}} - \underbrace{\int_0^y (-\overline{u'v'}) dy}_{\text{II}} \right]. \quad (18)$$

For instance, the decrease of  $U^{+0}$  around  $y^{+0} \simeq 10$  observed in Figure 7 can be explained as follows. In the decreasing cases (Cases A1 and A2), term I decreases by 7–8 %, while term II is nearly unchanged, as can be noticed from Figure 8(b). In Case B, term I increases by 11%, but term II increases more.

The rms velocity components are shown in Figure 9. In the drag reducing case (Case A1), the wall-normal component ( $v_{\text{rms}}$ ) is nearly unchanged, while the streamwise component ( $u_{\text{rms}}$ ) is reduced near the wall. This reduction of  $u_{\text{rms}}$  directly leads to the reduction of the RSS. In the drag increasing case (Case B),  $u_{\text{rms}}$  is also reduced. From this observation, the common effect of the present anisotropic compliant wall seems to be the reduction of the streamwise rms velocity and the enhancement of the wall-normal rms velocity. The reduction of the RSS (and the friction drag) seems to occur only when the  $v_{\text{rms}}$  induced by the wall-motion is not too large.

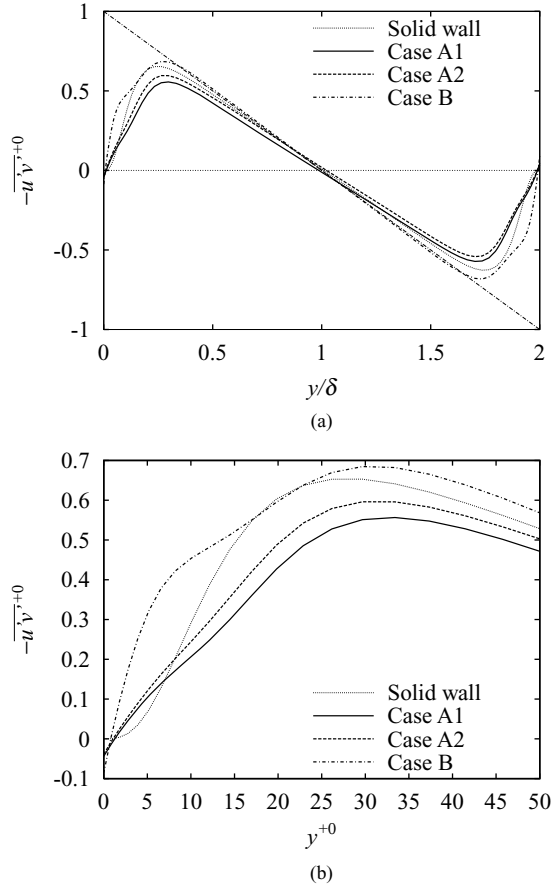


Figure 8. Reynolds shear stress: (a) overview; (b) near the wall.

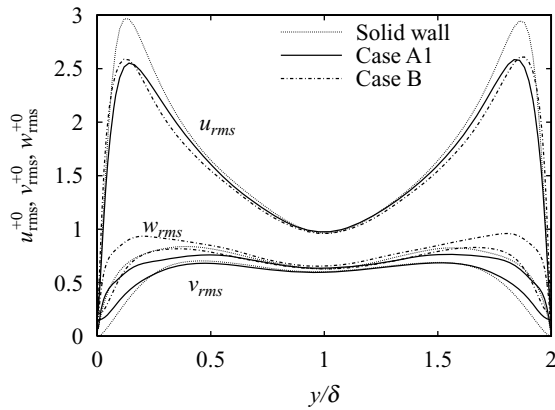


Figure 9. The rms velocity fluctuations.

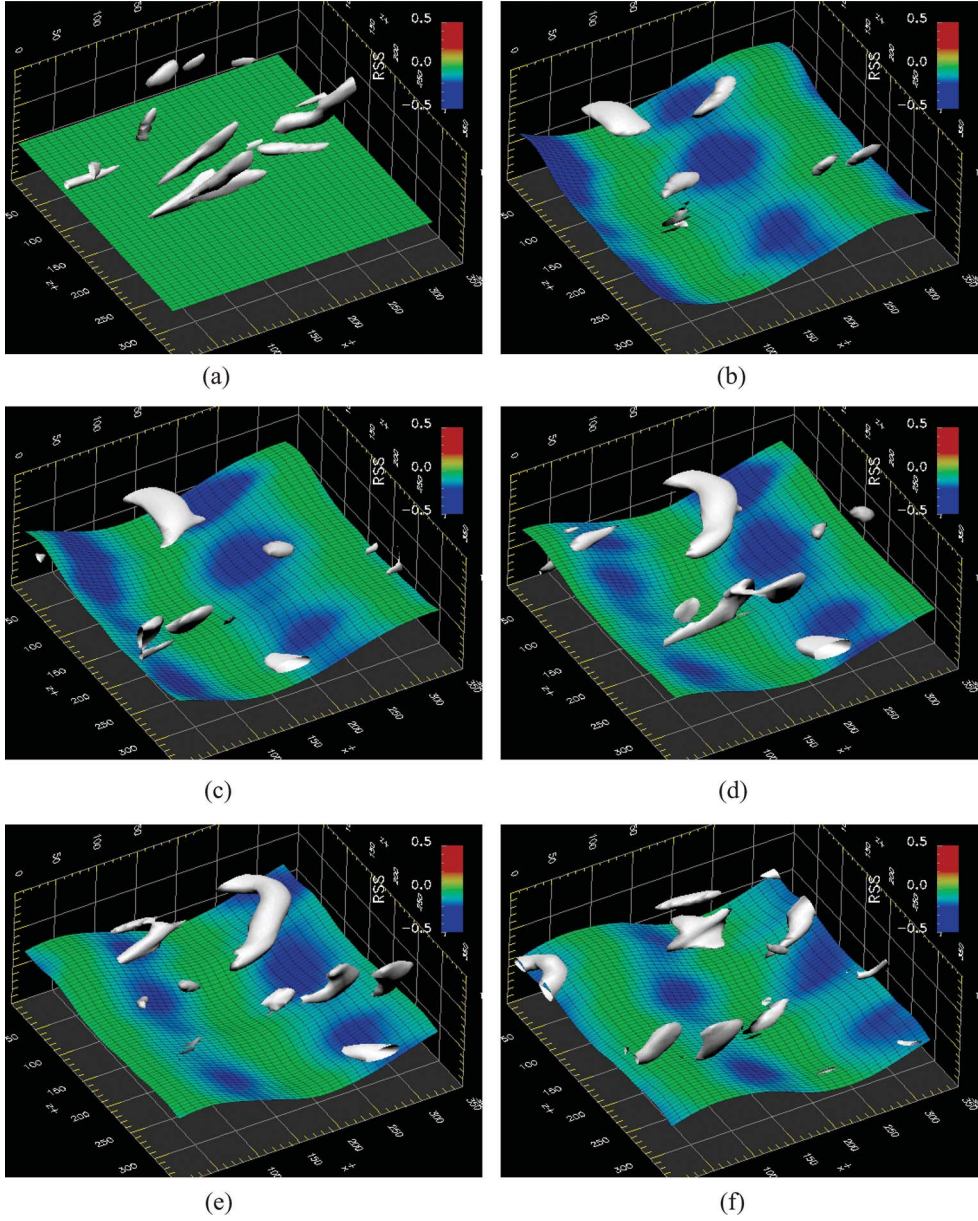


Figure 10. Wall motion (magnified by five times in the  $y$  direction), Reynolds shear stress (color on the wall), and vortical structure (white,  $Q^+ = 0.02$ ) in the drag-reducing case (Case A1). (a) Solid wall; (b)–(f) time sequence of compliant wall (time interval is about 7 wall units).

#### 4.3. Motion of the anisotropic compliant surface

Figure 10 shows the wall motion of the drag reducing case (Case A1). The surface deforms in a wavelike manner, which travels in the downstream direction. The wavelength is about 330 wall units (i.e., the same length as the computational domain) and the wavespeed is observed to be  $c^{+0} \simeq 4$ . In terms of the bulk velocity, this corresponds to  $c/U_b \simeq 0.3$ . The RSS on the wall

is made largely negative in front of and behind the hill where the wall-velocity is large (see, Equation (5)). The quasi-streamwise vortices observed on the solid wall (Figure 10(a)) are less populated on the compliant wall (Figures 10(b)–(f)), and instead, spanwise vortical structures are found to be increased. Such spanwise vortices have been observed also in other drag reducing flows under feedback control [23, 24]. Although its generation mechanism and its role in drag reduction are not fully clear, it is conjectured that they work as “rollers” between the wall and the bulk flow [23].

Koumoutsakos [23] reports traveling waves of blowing and suction as the result of a feedback vorticity flux control leading to large drag reductions. Recently, Min et al. [8] recovered the traveling-wave-like blowing and suction in DNS and demonstrated that this type of motion can generate a negative RSS near the wall, and thus, reduce the drag. We wish to emphasize at this point that our study achieves a similar motion with a passive device. Our optimal designs are somewhat in contradiction with those of Min et al. [8]. For blowing and suction control, the linear analysis of Min et al. [8] shows that downstream propagating waves always lead to a drag increase. Our results indicate the contrary for the present anisotropic compliant surface. The difference originates from the existence of a streamwise velocity component on the wall. While the negative RSS is caused by the phase difference between  $u'$  and  $v'$  in the case of Min et al. [8], the RSS on the wall is always made negative by the present anisotropic surface, as was illustrated in Figure 2 and Equation (5), and as was verified in Figure 8.

Figure 11 depicts the wall motion and turbulent structure in the drag increasing case (Case B). The wall motion is essentially similar to the drag reducing case, i.e., downward traveling wave with the wavelength about 330 wall units, but with a larger amplitude of deformation, as shown in Table 1. The wavespeed is found to be  $c^{+0} \simeq 6$ . The pattern of RSS on the wall is similar to that of the drag reducing case. The number of streamwise vortices, however, is observed to be drastically increased as compared to the case without control. The increase of streamwise vortices is qualitatively consistent with the increase of  $v_{\text{rms}}$ ,  $w_{\text{rms}}$ , and RSS observed above.

#### 4.4. Simulation in a larger computational domain

We performed simulations of Cases A1 and A2 in a computational domain doubled in the streamwise direction, i.e.,  $6\delta \times 2\delta \times 3\delta$ . The drag was not reduced, but doubled in both cases (i.e.,  $R_D \sim -200\%$ ). As shown in Figure 12, the surface deforms like a downward traveling wave similar to the cases in the original computational domain, but the wavelength is about 660 wall units (i.e., again, the same length as the computational domain) and the amplitude of deformation is about four times larger than the original case. The wavespeed is also found to be larger ( $c^{+0} \simeq 7$ ). Although the RSS is made negative on the wall, it is drastically increased in the rest of the channel, as shown in Figure 13. The wall-normal velocity fluctuation on the wall and the wall displacement are found to be  $v_{\text{rms}}^{+0} = 0.45$  and  $y_{\text{rms}}^{+0} = 6.5$ , respectively (Case A1). Similar to the argument made for Case B in Section 4.2, too large wall-normal velocity seems to have caused the increase of drag.

The present method and the findings discussed in the previous sections are limited, at the moment, to a small domain and small wall-deformation amplitudes. We find that applying optimal parameters obtained in a small domain to larger domains is not suitable and, in fact, it may lead to drag increase rather than drag reduction. This drag increase can be attributed to longer wavelength structures developing in the larger domains. We note that this observation is similar to the recent findings [25] indicating that the optimal controllers for two-dimensional bluff body flows are not necessarily optimal for the respective three-dimensional flows. Moreover, the unexpected result obtained in the larger domain may also be related to the validity of the assumption made on the wall deformation. These arguments imply that the optimization performed herein will need to be



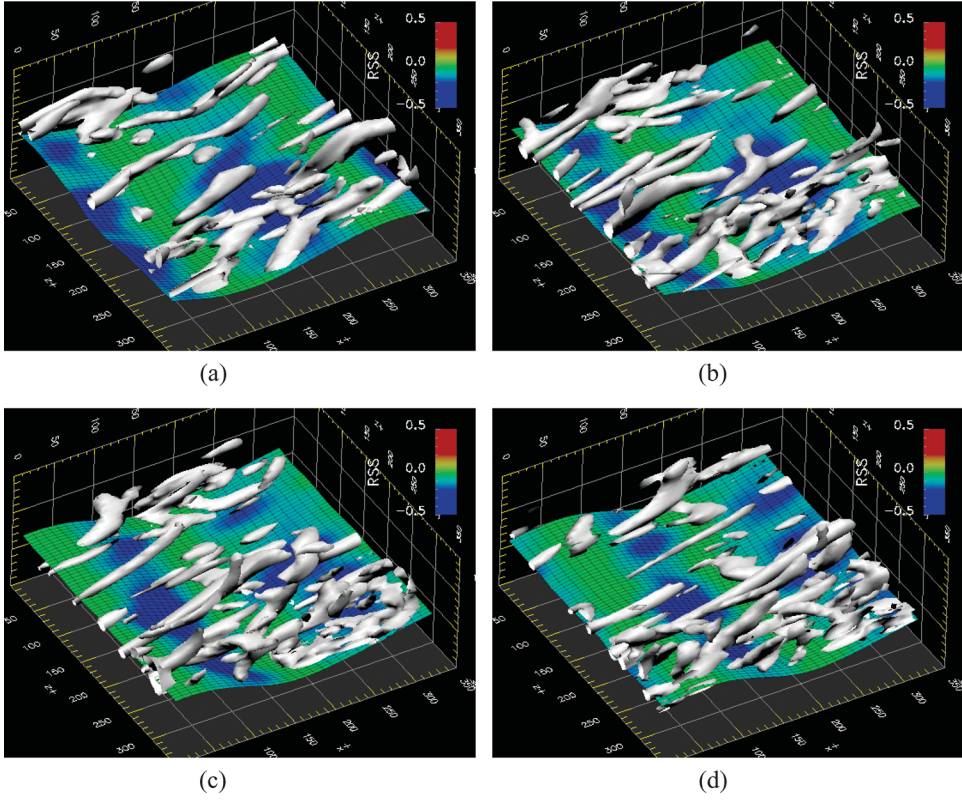


Figure 11. Time sequence of wall motion (magnified by five times in the  $y$  direction), Reynolds shear stress (color on the wall), and vortical structure (white,  $Q^+ = 0.02$ ) in the drag-increasing case (Case B). Time interval is about 7 wall units.

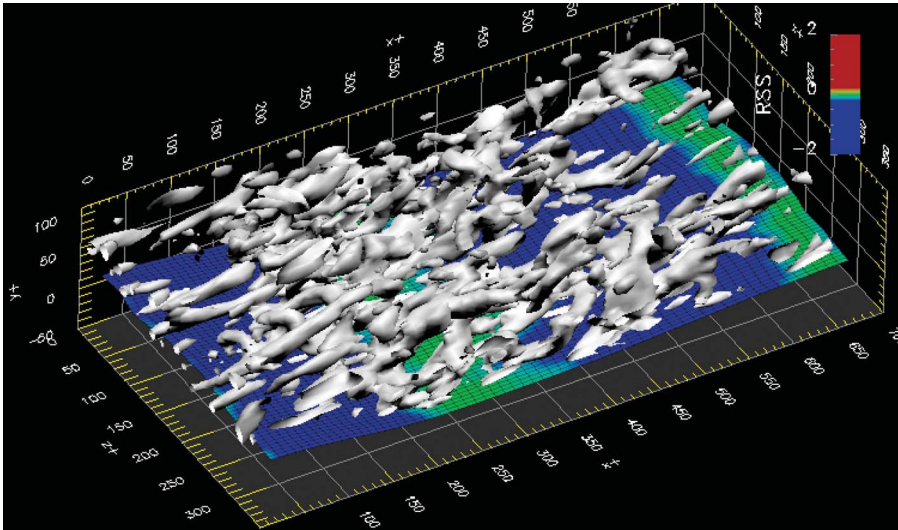


Figure 12. Wall motion (no magnification in the  $y$  direction), Reynolds shear stress (color on the wall), and vortical structure (white,  $Q^+ = 0.02$ ) in the doubled computational domain (Case A1).



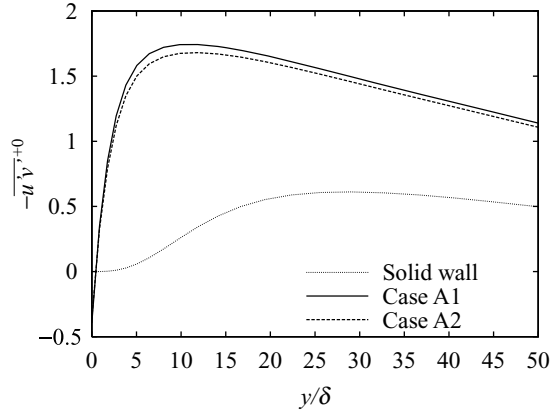


Figure 13. Reynolds shear stress in the case of doubled computational domain.

repeated in larger domains and with a different method to handle wall deformation. This approach requires significantly more computational resources and it is a subject of ongoing investigation.

## 5. Conclusions

We performed DNS of turbulent channel flow at  $Re_{\tau_0} \simeq 110$  with an anisotropic compliant surface. Unlike the isotropic compliant surface used in the previous DNS studies, the anisotropic compliant surface is driven by the streamwise wall-shear stress as well as by the wall pressure. Under the assumption of small deformation, the velocity of the compliant surface was fed back to the fluid velocity field as the wall boundary condition, while the effect of displacement was neglected.

For the optimization study, the computational domain was set to be  $3\delta \times 2\delta \times 3\delta$  in the streamwise, wall-normal, and spanwise directions, where  $\delta$  is the channel half-width. The CMA-ES was used to optimize five parameters and we obtain several sets of parameters that lead to reduction of the friction drag. The maximum drag reduction rate attained in the present optimization attempt is about 8%. The equilibrium arm angle of the drag reducing cases is found to be about  $60^\circ$ . This angle implies that the wall-shear stress, rather than the wall pressure, is an important driving force for the surface motion. Both in the drag reducing and drag increasing cases, the resultant surface motion is found to be a traveling wave traveling downstream. The Reynolds shear stress on the wall is found to become negative due to the motion of surfaces restricted by the inclined arms. We also observe a much reduced streamwise rms velocity component near the wall. The difference between the drag reducing and increasing cases is found in the wall-normal rms velocity component: it is kept at a level comparable to the one in the solid channel in the drag reducing case, while it is significantly increased in the drag increasing case.

Simulation was performed also in a computational domain doubled in the streamwise direction, i.e.,  $6\delta \times 2\delta \times 3\delta$ , using the two optimal sets of parameters obtained in the smaller domain. The drag is found to increase in both cases. The reason for this drag increase is attributed to the development of longer waves and the excessively large wall-normal velocity induced thereby.

The limitation of the present method is the necessity to use a small computational domain as well as to assume small deformation of the surface, which was necessary in order to perform a huge number of DNS runs for evolutionary optimization. While the present study demonstrates that the drag reduction by anisotropic compliant surfaces can be achieved by performing the optimization

of parameters, it also indicates that simply applying the optimal parameters obtained in the small domain to larger domains fails to reduce the drag.

## Acknowledgments

We would like to thank two anonymous reviewers for their constructive comments. We also wish to acknowledge support by the University of Tokyo—ETH Zürich exchange agreement. This work was partly supported by Keio Gijuku Academic Development Funds.

## References

- [1] M. Gad-el-Hak, *Compliant coatings for drag reduction*, Prog. Aerosp. Sci. 38 (2002), pp. 77–99.
- [2] T. Endo and R. Himeno, *Direct numerical simulation of turbulent flow over a compliant surface*, J. Turbulence 3(7) (2002), pp. 1–10.
- [3] S. Xu, D. Rempfer, and J. Lumley, *Turbulence over a compliant surface: Numerical simulation and analysis*, J. Fluid Mech. 478 (2003), pp. 11–34.
- [4] P.W. Carpenter and P.J. Morris, *The effect of anisotropic wall compliance on boundary-layer stability and transition*, J. Fluid Mech. 218 (1990), pp. 171–223.
- [5] K. Fukagata, K. Iwamoto, and N. Kasagi, *Contribution of Reynolds stress distribution to the skin friction in wall-bounded flows*, Phys. Fluids 14 (2002), pp. L73–L76.
- [6] T.R. Bewley and O.M. Aamo, *A “win-win” mechanism for low-drag transients in controlled 2D channel flow and its implications for sustained drag reduction*, J. Fluid Mech. 499 (2004), pp. 183–196.
- [7] K. Fukagata and N. Kasagi, *Suboptimal control for drag reduction via suppression of near-wall Reynolds shear stress*, Int. J. Heat Fluid Flow 25 (2004), pp. 341–350.
- [8] T. Min, S.M. Kang, J.L. Speyer, and J. Kim, *Sustained sub-laminar drag in a fully developed channel flow*, J. Fluid Mech. 558 (2006), pp. 309–318.
- [9] K. Fukagata and N. Kasagi, *Highly energy-conservative finite difference method for the cylindrical coordinate system*, J. Comput. Phys. 181 (2002), pp. 478–498.
- [10] K. Fukagata, N. Kasagi, and P. Koumoutsakos, *A theoretical prediction of friction drag reduction in turbulent flow by superhydrophobic surfaces*, Phys. Fluids 18 (2006), pp. 1–4.
- [11] T. Kajishima, *Finite-difference method for convective terms using non-uniform grid*, Trans. JSME/B 65 (633) (1999), pp. 1607–1612 (in Japanese).
- [12] F.E. Ham, F.S. Lien, and A.B. Strong, *A fully conservative second-order finite difference scheme for incompressible flow on nonuniform grids*, J. Comput. Phys. 177 (2002), pp. 117–133.
- [13] P.R. Spalart, R.D. Moser, and M.M. Rogers, *Spectral methods for the Navier–Stokes equations with one infinite and two periodic directions*, J. Comput. Phys. 96 (1991), pp. 297–324.
- [14] J.K. Dukowicz and A.S. Dvinsky, *Approximate factorization as a higher-order splitting for the implicit incompressible flow equations*, J. Comput. Phys. 102 (1992), pp. 336–347.
- [15] S. Kang and H. Choi, *Active wall motions for skin-friction drag reduction*, Phys. Fluids 12 (2000), pp. 3301–3304.
- [16] J. Miwa, *Control of wall-turbulence by shell-deformable actuators*, M.Eng. thesis, The University of Tokyo, 2003, 109 pp. (in Japanese).
- [17] N. Hansen and A. Ostermeier, *Completely derandomized selfadaptation in evolution strategies*, Evol. Comput. 9 (2001), pp. 159–195.
- [18] N. Hansen, S.D. Müller, and P. Koumoutsakos, *Reducing the time complexity of the derandomized evolution strategy with covariance matrix adaptation (CMA-ES)*, Evol. Comput. 11 (2003), pp. 1–18.
- [19] N. Hansen and S. Kern, *Evaluating the CMA evolution strategy on multimodal test functions*, Parallel Probl. Solving Nat.—PPSN VIII (2004), pp. 282–291.
- [20] S. Kern, S.D. Müller, N. Hansen, D. Büche, J. Ocenasek, and P. Koumoutsakos, *Learning probability distributions in continuous evolutionary algorithms—a comparative review*, Nat. Comput. 3 (2004), pp. 77–112.
- [21] K. Fukagata and N. Kasagi, *Drag reduction in turbulent pipe flow with feedback control applied partially to wall*, Int. J. Heat Fluid Flow 24 (2003), pp. 480–490.
- [22] N. Kasagi and K. Fukagata, *The FIK identity and its implication for turbulent skin friction control*, in *Transition and Turbulence Control*, M. Gad-el-Hak and H.M. Tsai, eds., World Scientific, Singapore, 2006, pp. 297–324.

- [23] P. Koumoutsakos, *Vorticity flux control in a turbulent channel flow*, Phys. Fluids 11 (1999), pp. 248–250.
- [24] K. Fukagata, N. Kasagi, and K. Sugiyama, *Feedback control achieving sublamina friction drag*, in *Proceedings of the 6th Symposium on Smart Control of Turbulence*, Tokyo, March 6–9, 2005, pp. 143–148.
- [25] Ph. Poncet, R. Hildebrand, G.H. Cottet, and P. Koumoutsakos, *Spatially distributed control for optimal drag reduction of the flow past a circular cylinder*, J. Fluid Mech. 599 (2008), pp. 111–120.